Effects of microporous layer on electrolyte flooding in gas diffusion electrodes and selectivity of CO_2 electrolysis to CO

Wu, Yuming; Garg, Sahil; Li, Mengran; Idros, Mohamed Nazmi; Li, Zhiheng; Lin, Rijia; Chen, Jian; Wang, Guoxiong; Rufford, Thomas E.

DOI
10.1016/j.jpowsour.2022.230998

Publication date
2022

Document Version
Final published version

Published in
Journal of Power Sources

Journal of Power Sources 522 (2022) 230998

Contents lists available at ScienceDirect

Journal of Power Sources

journal homepage: www.elsevier.com/locate/jpowsour

Effects of microporous layer on electrolyte flooding in gas diffusion electrodes and selectivity of CO_2 electrolysis to CO

Yuming Wu [a], Sahil Garg [b], Mengran Li [c,**], Mohamed Nazmi Idros [a], Zhiheng Li [a], Rijia Lin [a], Jian Chen [a], Guoxiong Wang [a], Thomas E. Rufford [a,*]

[a] School of Chemical Engineering, The University of Queensland, St Lucia, 4072, Australia
[b] Section for Surface Physics and Catalysis, Department of Physics, Technical University of Denmark, 2800 Kgs, Lyngby, Denmark
[c] Materials for Energy Conversion and Storage (MECS), Department of Chemical Engineering, Faculty of Applied Sciences, Delft University of Technology, van der Maasweg 9, 2629, HZ Delft, The Netherlands

HIGHLIGHTS

- A facile method was firstly reported to quantify catholyte flooding by CO_2RR.
- The MPL plays a crucial role in preventing flooding and supporting catalyst layer.
- A thin MPL allows more local CO_2 on the catalyst layer at low current densities.
- A thick MPL considerably suppresses electrolyte flooding at high current densities.

GRAPHICAL ABSTRACT

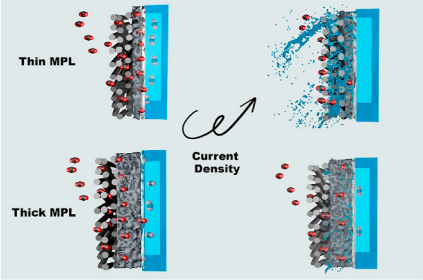

ARTICLE INFO

Keywords:
Electrochemical CO_2 reduction
Gas diffusion electrode
Microporous layer
Thickness
Electrolyte flooding

ABSTRACT

Understanding the relationship between gas diffusion electrode (GDE) structures and the performance of electrochemical CO_2 reduction reaction (CO_2RR) is crucial to developing industrial-scale technologies to convert CO_2 to valuable products. We studied how the microporous layer (MPL) on GDE's coated with silver nanoparticle catalysts affects the electrochemical CO_2 conversion to CO in a flow cell electrolyser. We demonstrate a convenient method to measure the rate of catholyte seepage through a GDE during CO_2RR experiments and used this method to show how the MPL thickness affects flooding of the GDE. We found the GDE with the thickest MPL (39BB) had the best selectivity for CO and stability at current densities above 100 mA cm^{-2} as the thick MPL minimized flooding. However, at low current densities the 39BB electrode achieved a lower CO selectivity than the GDE with thinner MPL. These results suggest opportunities to improve CO_2 electrolyser performances at high current by optimisation of the MPL structure and wettability.

; CO_2RR, CO_2 reduction reaction; GDE, gas diffusion electrode; GDL, gas diffusion layer; MPL, microporous layer; CFS, carbon fibre support; CL, catalyst layer; PTFE, polytetrafluoroethylene; AgNP, silver nanoparticles; FE, Faradaic efficiency.

* Corresponding author.
** Corresponding author.
E-mail addresses: m.li-8@tudelft.nl (M. Li), t.rufford@uq.edu.au (T.E. Rufford).

https://doi.org/10.1016/j.jpowsour.2022.230998
Received 14 September 2021; Received in revised form 9 December 2021; Accepted 9 January 2022
Available online 15 January 2022

1. Introduction

The electrochemical CO_2 reduction reaction (CO_2RR) powered by renewable electricity opens up new possibilities to convert CO_2 in industrial waste gases to chemical feedstocks or fuels [1–3]. For example, CO_2 produced in cement or steel-making industries could be converted to carbon monoxide (CO), formic acid, or methanol. In recent years there have been significant advances in highly selective catalyst materials for electrochemical CO_2 reduction (for example, see reviews by Berlinguette et al. [4] and Dong et al. [5]). Continuous high-current density electrolysers using gas diffusion electrodes (GDEs) [6] have moved towards pilot-scale demonstrations [7].

The critical difference between GDEs in continuous electrolysers and simpler electrodes in a H-type electrochemical cell is that in a GDE [8,9], the CO_2 gas diffuses through a porous gas diffusion layer (GDL), then diffuses through a liquid film to the active sites in the catalyst layer (CL), as shown in Fig. 1. This improvement in CO_2 mass transport allows electrolysers with GDEs to achieve current densities above 100 mA cm^{-2} required for economically viable CO_2 conversion at industrial scales [10]. A typical commercial GDL consists of a carbon fiber support (CFS) and a microporous layer (MPL), with the catalyst coated on this MPL. The microporous layer is typically carbon black mixed with hydrophobic polytetrafluoroethylene (PTFE) [11] to mitigate electrolyte flooding into the porous GDE [12]. The distance that the liquid electrolyte penetrates, or floods into the MPL and CFS layers can significantly impact the effectiveness of the GDE to enhance transport of CO_2 to active catalysts sites, and therefore also impact overall CO_2RR performance [13].

Commercial GDEs with platinum-group catalysts for the oxygen reduction reaction (ORR) have for some time been used in polymer electrolyte membrane (PEM) fuel cells and are studied for other reactions like acetylene reduction [14]. Although the science of GDEs for PEM fuel cells is well advanced [15], there are critical differences in conditions for the ORR in a fuel cell and the CO_2RR [6] that will impact design and performance requirements for GDEs. For example, (1) the ORR produces OH^- but CO_2RR can produce liquid products that lower surface tension [16]; (2) directing the selectivity of CO_2RR is more challenging than ORR over platinum because a wide range of CO_2RR products plus the H_2 evolution reaction occur at similar equilibrium potentials [17], (3) consequently, CO_2RR is highly sensitive to local pH and CO_2 concentrations at the catalyst sites [10,18]; and (4) the properties of catalysts for CO_2RR (e.g., Cu, Sn-based, or Ag) are more easily affected by CO_2RR conditions [19,20] than platinum-group metals.

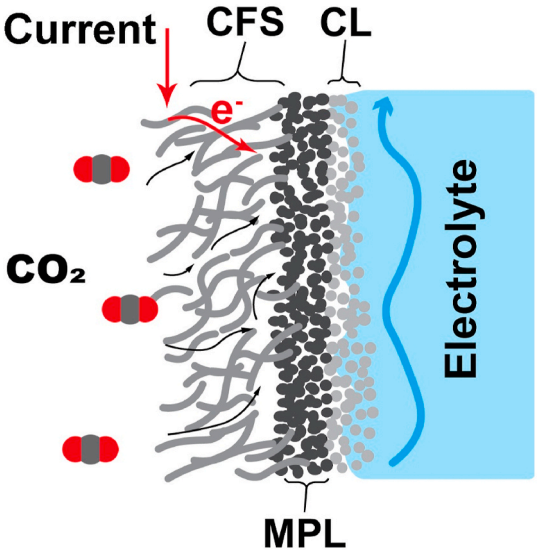

Fig. 1. A schematic of gas diffusion electrode for CO_2 electrolysis with a carbon fiber support (CFS), microporous layer (MPL), and catalyst layer (CL).

Given these critical differences there is a need to better understand GDE performance in CO_2RR so we can tailor electrode and catalyst layer design and manufacture.

Several studies report the effects of the MPL on PEM fuel cell performance [21–24]. Yet, the effects of MPL and GDE structures on the more complex CO_2RR are less well understood than for PEM fuel cells. There are very few studies in this space, notably the report from Kim et al. [25] that study the effects of MPL and CFS compositions of CO_2RR performance. We investigated the effect of MPL thickness on CO_2 electrolysis to CO over silver nanoparticles (AgNPs) using four commercial GDLs in a gas-fed flow cell electrolyser. First, we demonstrate a convenient method to measure the rate of catholyte seepage through a GDE during CO_2RR experiments, and then we used this method to show how the MPL thickness affects flooding of the GDE. We found the GDE with the thickest MPL (39BB) had the best selectivity for CO and stability at current densities above 100 mA cm^{-2} as the thick MPL minimized flooding. However, the 39BB electrode achieved a lower CO selectivity at low current densities than the GDE with thinner MPL. These results suggest a trade-off at high current densities when using thicker MPLs between the benefits of mitigating flooding and increased resistance to CO_2 gas transfer to the catalyst layer.

2. Materials and methods

2.1. Gas diffusion electrodes preparation

The four commercial GDLs were 29AA, 22BB, 36BB, and 39BB from SIGRACET®. We choose these materials because similar SIGRACET® gas diffusion layers are reported in other CO_2RR studies [26–29] and GDE flooding studies for PEM fuel cells, including a study by Lin and Nguyen, Lin and Nguyen [30] on the effect of GDE thickness on flooding. The thicknesses of the GDLs measured by a micrometer thickness gauge ranged from 125 μm to approximately 300 μm (Table 1). The 22BB, 36BB, and 39BB materials all have an MPL plus the carbon fiber support, and the 125 ± 1 μm thick 29AA has only the carbon fiber support layer with no added MPL. The GDLs were cut into 3 cm × 3 cm square pieces for electrode studies.

We prepared cathode GDEs by spraying an ink of AgNPs, carbon black (as catalyst supporter), and perfluorinated resin (mainly function as proton conduction) in isopropyl alcohol onto the MPL side of the gas diffusion layers. The catalyst ink contained 100 mg AgNPs (99.9%, 20–40 nm, Thermo Fisher Scientific, example TEM image in Fig. S3a of the Supporting Information), 100 mg carbon black (CB, 99%, Thermo Fisher Scientific), 1 mL perfluorinated resin solution (Nafion, 5 wt% resin, Sigma Aldrich), and 4 mL isopropyl alcohol (IPA, ≥99.7%, Sigma Aldrich). This mixture was sonicated for 30 min before spray coating. The ink was sprayed onto the MPL using a manual airbrush (RS PRO Air Brush Kit, with 0.3 mm Tip) with a fixed airflow, and then the electrodes were dried at 100 °C to vaporize IPA and water. The silver-based catalyst loadings confirmed by the GDE weights before and after spray coating were 1.0 ± 0.1 mg cm^{-2} of AgNPs + CB + perfluorinated resin on GDEs. For 29 AA, the catalyst was sprayed on the carbon fibre support directly. Throughout this manuscript, we refer to the catalyst coated materials as the gas diffusion electrode (GDE), and the as-received commercial gas diffusion layers as GDL.

Table 1
The thickness of the commercial GDLs measured by micrometer gauge and estimated from SEM images.

GDLs	Thickness from micrometer gauge μm	Thickness based on SEM μm
29AA	125 ± 1	119 ± 5
22BB	217 ± 1	223 ± 9
36BB	234 ± 1	225 ± 12
39BB	301 ± 6	264 ± 11

2.2. Contact angles measurement

Sessile drop contact angles of deionised water and 0.5 M $KHCO_3$ solution in air were measured by a goniometer using a 3 Megapixel CMOS digital camera with a 50 mm Nikon lens and a 12 V light source. We determined the contact angles from the images using a purpose-built image analysis algorithm (code available at Idros [31]). We used a 1–10 μL volume pipette to dispense 5 ± 0.2 μL of liquid at least three locations on each MPL surface. The error bars shown in the contact angle results represent the variation in these repeated measurements. To measure contact angles on the GDEs after use in the CO_2RR, we dissembled the electrolyser and rinsed the GDE with deionised water to remove residual electrolyte from the MPL surface.

2.3. Gas permeance measurement

We used a custom-built gas permeation apparatus to measure the permanence of GDEs (details available in Ge et al. [32]). The GDEs were secured between two plates to ensure a gas-tight seal during the experiment. The CO_2 gas was fed through the sample from the CFS side to the CL side at a fixed flow rate with the resultant pressure drop across the GDE measured. We measured the flow rate at the outlet of the CL side using a digital flow meter. We recorded the pressure drop at five different flow rates for each sample and repeated the measurements with three samples of each GDE.

The permanence P ($m.s^{-1}Pa^{-1}$), was calculated using Eq. (1):

$$p = \frac{q}{A \times (p_{inlet} - p_{outlet})} \quad (1)$$

Where q ($m^3\ s^{-1}$) is the flow rate, A (m^2) is the measured area of GDE, p_{inlet} (Pa) is the pressure of the inlet side of GDE, and p_{outlet} (Pa) is the pressure of the outlet side of GDE.

2.4. Other materials characterization methods

Scanning electron microscopy (SEM) and energy-dispersive X-ray spectroscopy (EDS) were performed on a JOEL JSM-7001F instrument. Transmission electron microscopy (TEM) images were collected with a Hitachi HT 7700. The pore size distributions of each GDL were characterised by mercury intrusion porosimetry (MIP, Micromeritics AutoPore IV 9500).

2.5. Electrochemical measurement

The CO_2RR experiments were performed in a gas-fed flow cell electrolyser with a single-pass catholyte flow, which was purchased from ElectroCell A/S, Denmark prior to modification and design for purpose of our requirement, as shown in Fig. 2a and Fig. S4. All of electrochemical measurement was controlled by a Metrohm Autolab PGSTAT302 N potentiostat. The AgNP decorated GDE was the cathode, an IrO_2 coated titanium plate (commercial DSA® anode from ElectroCell A/S, Denmark) was the anode, and an Ag|AgCl was used as a reference electrode (as shown in Fig. S4a). The cathode area exposed to the

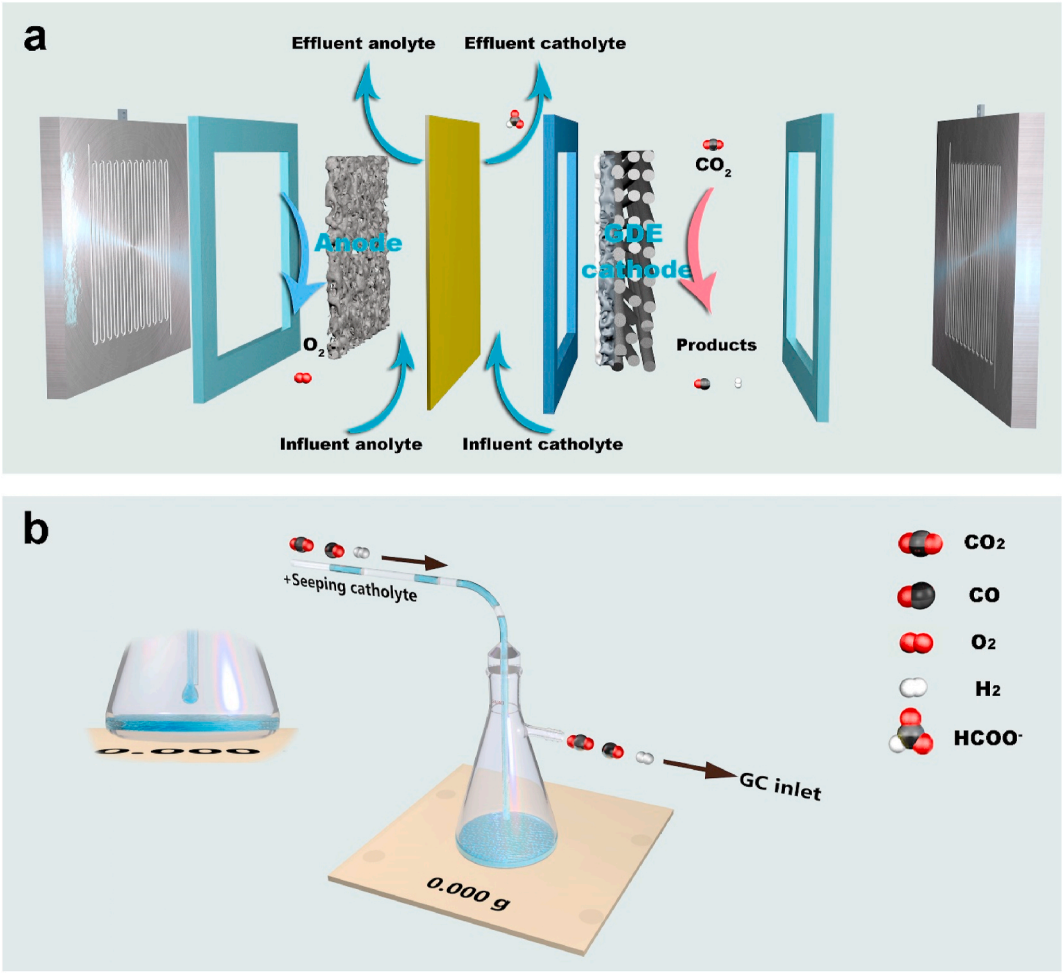

Fig. 2. Schematic diagram of (a) the flow-cell electrolyser during CO2RR and (b) the seepage rate measurement.

catholyte was a 2 cm × 2 cm square. The catholyte and anolyte were both 0.5 M $KHCO_3$ solutions and separately pumped at 1 mL min^{-1} into corresponding chambers in single-pass to minimize local accumulation of products. The anode and cathode half-cells were separated by a Nafion 117 membrane (from FuelCellStore). Before testing, the catholyte was purged with CO_2 for at least 30 min.

2.6. Seepage rate measurement

We measured the rate of catholyte seepage by separating and collecting any liquid carried out with gases from the cathode chamber in a two-neck Erlenmeyer flask placed on an analytical balance (Fig. 2b and Fig. S4c). This flask was positioned upstream of the gas chromatograph, with all reactor outlet tubing designed to minimize pressure drop. We recorded the liquid mass collected in the flask at least three times at each measured current density and calculated a mean liquid seepage rate.

2.7. Product analysis

The compositions of gas products were analysed with a Shimadzu GC-2030 gas chromatograph with a ShinCarbon packed column (ST 80/100, 2 mm ID, 1/8 OD Silco, Restek) and a thermal conductivity detector (TCD) and a flame ionization detector (FID). Hydrogen (H_2, 99.999%, BOC Australia) and argon (Ar, 99.999%, Supagas Australia) were used as the carrier gases for the FID and the TCD, respectively. Air was used as the balance gas for the FID. The GC was calibrated using a standard calibration gas of 10% H_2 and 10% CO balanced with Ar.

The Faradaic efficiencies (FE_i) of CO and H_2 were calculated by:

$$FE_i = \frac{p \times v \times c_i \times F \times N_i}{R \times T \times j} \times 100\% \quad (2)$$

where p is 101.31 kPa, v is the flow rate of effluent gas measured using a digital flowmeter (Optiflow 520, Sigma Aldrich), c_i is the concentration of the gas product species i measured by the GC, F is the Faraday constant (96,485 C mol^{-1}), $N_i = 2$ is the number of electrons transfer for 1 mol CO_2RR product for both H_2 and CO, R is the gas constant (8.31446 J K^{-1} mol^{-1}), T is the temperature of CO_2RR reactor, and j is the total current recorded by the potentiostat.

We analysed the liquid products with nuclear magnetic resonance (NMR) ^{1}H spectroscopy (Bruker Avance 500 high-resolution NMR). Liquid samples were prepared for the NMR analysis by mixing 400 μL of the effluent liquid from the cathode chamber in 200 μL of heavy water (D_2O, 99.9 atom% D, Sigma Aldrich) mixed with 0.05 vol% dimethyl sulfoxide (DMSO, ≥ 99%, Sigma Aldrich) as the internal standard. Then the concentrations of liquid products were determined from the mass ratio between liquid products and DMSO. Finally, the FE of liquid (FE_l) products were calculated by the following equation:

$$FE_l = \frac{c_l \times v_{catholyte} \times F \times N_i}{j} \times 100\% \quad (3)$$

where c_l is the concentration of the liquid product, $v_{catholyte}$ is the flow rate of catholyte displayed on the pump's LCD screen), and the other variables are defined the same as in Eq. (1).

3. Results and discussion

3.1. Characterization of the carbon gas diffusion layers

The SEM images of the cross-sections of the GDLs in Fig. 3 a-d show the thickness of the carbon fibre support and microporous layers in each commercial GDL. We used these SEM images to estimate the thicknesses of the carbon fibre support and microporous layers, following a method reported by Tan, Lee, Song and Oh [33]). These results are summarised in Fig. 3e. All four GDLs from SIGRACET® have the same base CFS, and our SEM analysis gave a CFS thickness of approximately 120 μm, which is consistent with the 125 μm thickness of 29AA measured by the micrometer gauge (Table 1). Following that confirmation of CFS thickness, we estimate the thicknesses of the MPLs to be 223 ± 9 μm in 22BB, 225 ± 12 μm in 36BB, and 264 ± 11 μm in 39BB (Fig. 3e).

Fig. 3f shows the pore size distribution of the GDLs determined from mercury intrusion porosimetry (MIP). All four GDLs have a large volume of pores with a size in the range of 10–182 μm according to the MIP, and

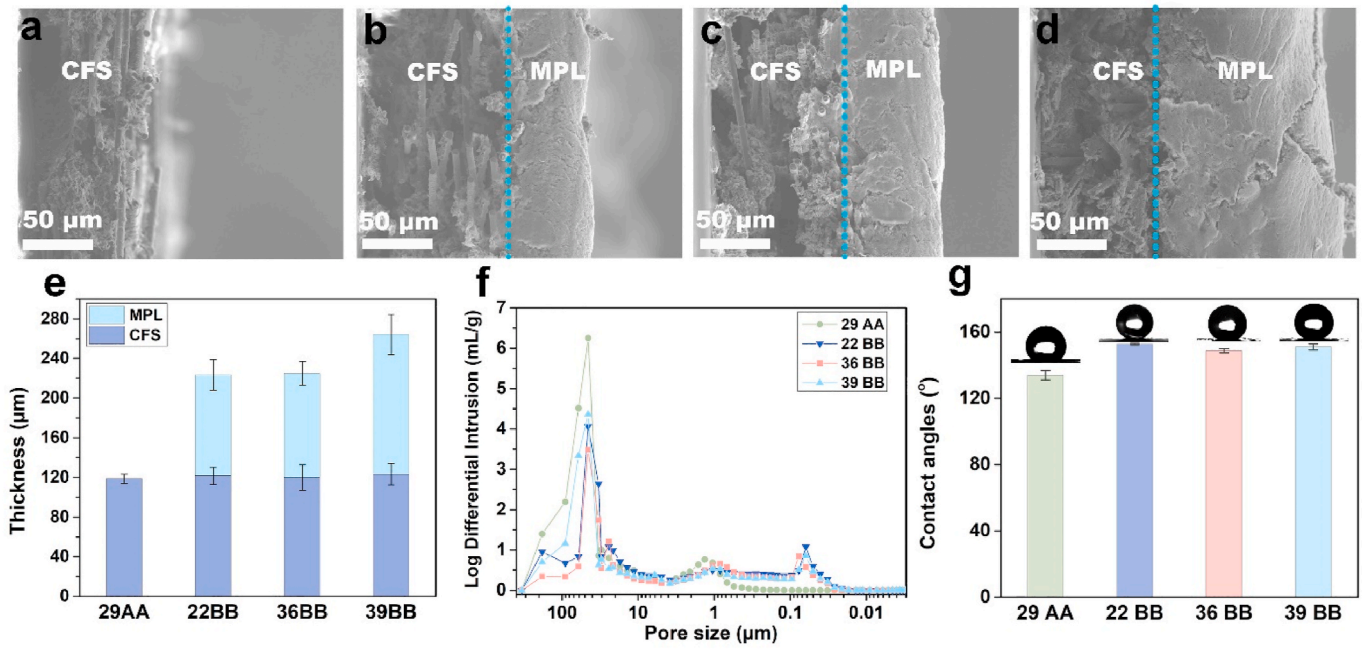

Fig. 3. Cross-sectional morphologies of the commercial (a) 29AA, (b) 22BB, (c) 36BB and (d) 39BB; (e) Measured thicknesses of CFS and MPL of the commercial GDLs (the statistical data was obtained through SEM image analyzing, and the error bars represent the standard deviation of 12 measurements, three areas of each four separate samples); (f) Pores size distribution of the commercial GDLs obtained from mercury intrusion porosimetry; (g) Sessile drop apparent contact angles of water in the air on the MPL side of the commercial GDLs.

these pore sizes are consistent with the voids between the network of fibers in the CFS layer (see SEM image in Fig. S1a). The pore size distributions are consistent with MIP data reported in the literature for similar GDLs [34,35]. The corresponding cumulative pore size distribution is shown in Fig. S2. As expected, the pore size distribution for 29AA in Fig. 3f shows a fewer pores smaller than 1 μm than the pore size distributions of the three GDLs with MPLs. The SEM images provided in the Supporting Information show that the surfaces of the MPLs (Figs. S1b–d) were much flatter than the CFS of 29AA (Fig. S1a). The MPL surfaces also have large cracks (Figs. S1b–d) that likely formed during the sintering and cooling cycles used to deposit the MPL on the CFS in the GDLs manufacturing process [36]. In PEM fuel cells, these cracks have been observed to influence flooding [37], and we expect the cracks could have a similar impact in a CO_2 electrolyser.

Fig. 3g shows that the apparent contact angles measured by the Sessile drop method are approximately 13° larger on the MPL of 22BB, 36BB, and 39BB than on the CFS surface of 29AA ($\theta = 133.9 \pm 2.5°$). These results are because the MPLs have a higher loading of PTFE and smaller pores than the carbon fibre support. The apparent contact angles we measured are similar to results reported by others using similar SIGRACET® GDLs [38].

3.2. Characterization of silver-coated gas diffusion electrodes

Fig. 4 parts (a) to (d) show the cross-sectional SEM images of the catalyst-decorated GDEs and the distribution of Ag and fluorine (F) in the electrode mapped by EDS. Fluorine was present in the PFTE used to fabricate the MPL and CFS in the commercial GDLs, and in the Nafion ionomer, we added with the catalyst. The Ag EDS map in Fig. 4a shows that the AgNPs penetrate deeper into the carbon fiber support of 29AA than they do in the MPL coated electrodes, as evidenced by a higher intensity of Ag signal observed in a thin layer at the right-hand side of the GDEs. Further evidence of the location of AgNPs in the GDEs is provided in the SEM images of the top surfaces of the catalyst layer in Fig. S3. Fig. S3c of AgNP on 36BB also shows that the AgNPs do not entirely cover or fill the cracks on the surface of the MPL, so these MPL cracks could still be open to gas and liquid flows. The apparent contact angles of water on the catalyst decorated GDEs (Fig. 4e) indicate that the catalyst-coated GDE remains hydrophobic. This observation is consistent with contact angles on Pt-decorated SIGRACET® GDLs reported by Ungan and Bayrakçeken Yurtcan [39].

Fig. 4f shows the CO_2 gas-phase through-plane permeance through 29AA was larger than the permeance through the three GDE with the microporous layers. The thickest electrode, 39BB, exhibited the most resistance to CO_2 transport. We note that these gas-phase permeance measurements do not precisely represent the conditions in the electrolyser where pores of the GDE will be partially filled with liquid electrolyte. Still, these measurements do provide some indication of the relative resistances to gas transport in each GDL.

3.3. The role of the microporous layer in CO_2RR

In the first set of electrochemical measurements to assess the CO_2RR to CO using the commercial GDLs as cathodes in the flow-cell electrolyser (Fig. 2a), we compared the performance of 29AA and 36BB. These GDLs have similar thickness carbon fibre supports, but the 29AA does not include an MPL (Fig. 3e), so this comparison allows us to investigate the role of the MPL. Fig. 5a shows the selectivity of CO_2RR to CO for 36BB was $FE_{CO} = 95\%$ at 25 mA cm^{-2} then decreased to $FE_{CO} = 70\%$ at 150 mA cm^{-2}. These results are similar to the FE_{CO} reported by García de Arquer et al. [40] for Ag nanoparticles on carbon GDEs (reported as a control experiment in their supporting information). The FE_{CO} of 29AA was only 13% at 25 mA cm^{-2}, and in the high current density range, there was very little CO produced with the 29AA GDE. Instead, the production of H_2 with the 29AA GDE was over 60% across the tested current densities and was much higher than the HER observed with the 36BB GDE. The $HCOO^-$ generated at the 36BB cathode is also shown in Fig. 5c, and the FE_{HCOO^-} increases with current density. Moreover, the

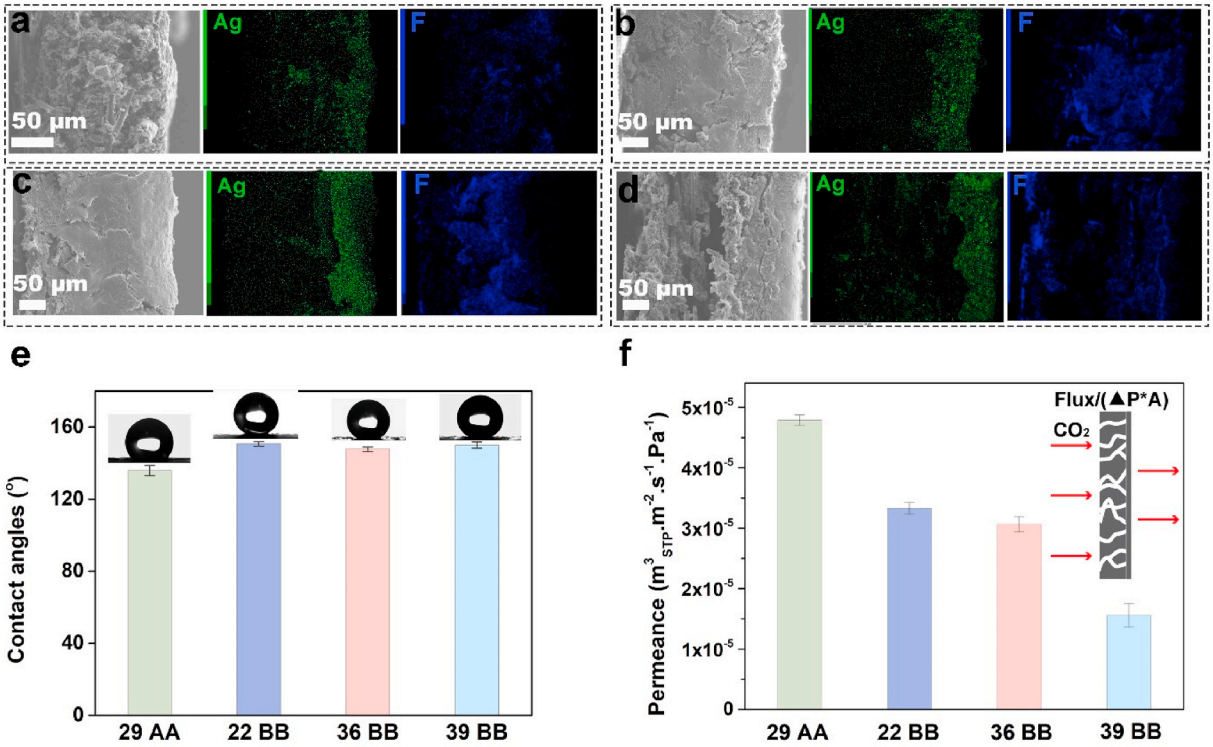

Fig. 4. Cross-sectional morphologies and EDS mapping results Ag and F on the GDEs loaded with 1.0 mg cm^{-2} AgNPs + carbon black + perfluorinated resin. (a) 29AA, (b) 22BB, (c) 36BB, and (d) 39BB. (e) Sessile drop contact angles of water in the air on catalyst layer/microporous layer side of the GDEs; and (f) through-plane permeance of CO_2 in the GDEs.

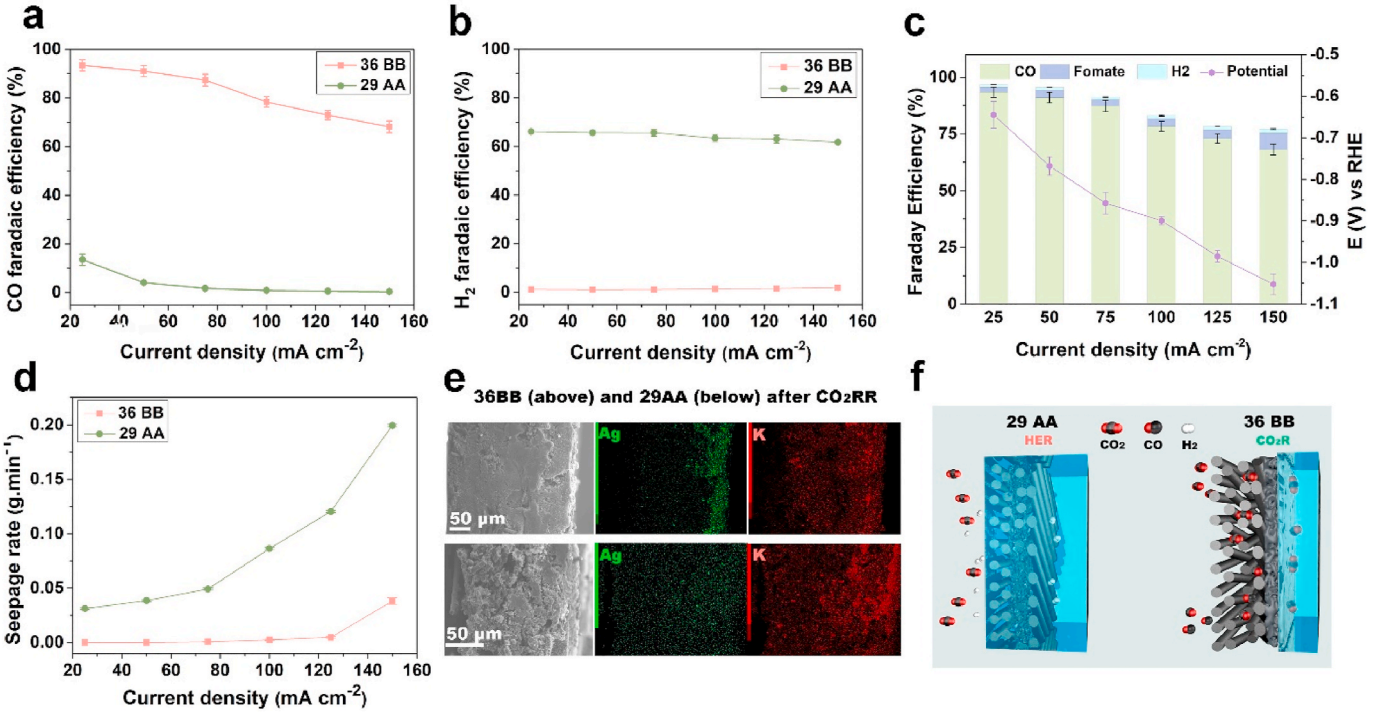

Fig. 5. Performance of the GDEs (with and without MPL) on CO2RR: (a) selectivity of CO, (b) H_2 and (c) 36BB overall depend on current density; (d) Flooding condition of the GDEs; (e) EDS mapping results of 36BB and 29AA after CO_2RR at 150 mA cm^{-2} for 60 min; (f) Illustration of how MPL works. The error bars represent the standard deviation of at least three independent measurements.

total faraday efficiency we observed is lower than 100% at high current densities, where the gas products (e.g., CO and H_2) may not be fully collected from the gas chamber and then detected by the GC. Such imperfection is related to the imbalanced gas/liquid pressures across the GDE likely due to electrode flooding. The phenomenon of less than 100% FE is a common issue for other studies [41,42]. These results confirm that the MPL plays a significant role in the enhancement of selectivity of CO_2RR. The higher CO_2RR selectivity over 36BB with MPL compared to 29AA GDE could be related to several factors, including (i) the role of MPL to prevent catholyte flooding and (ii) increased loss of AgNPs from the 29AA.

Fig. 5d shows an increase of seepage rate with current density for 29AA and 36BB. The increasement is owing to the larger surface charge density that would induce more negative adsorption energy between cathode and water, indicating a stronger interaction between the catholyte and cathode surface [43]. Thus, the developed hydrophilicity means easier wetting on the cathode surface. Moreover, it also shows the rate of catholyte seepage through 29AA was 0.20 g min^{-1} during CO_2RR experiments at a current density of 150 mA cm^{-2}. That is, approximately 20% of the catholyte pumped into the cathode cell (1 mL min^{-1}) of the electrolyte flowed through the GDE, and thus this condition represents an extreme case of electrode flooding. We expect a significant volumetric fraction of the pores in GDE to be filled with catholyte at this condition (Fig. 5f). This flooding will inhibit the diffusion of CO_2 in the GDE and starve the CL of CO_2, which leads to poor FE_{CO} as shown in Fig. 5a. For the 36BB GDE, catholyte seepage was only observed at current densities of 125 and 150 mA cm^{-2}, and even at 150 mA cm^{-2} the seepage rate was only 0.04 g min^{-1} (less han 5% of the catholyte pumping rate). This result suggests that at current densities up to 100 mA cm^{-2}, electrolyte flooding into the 36BB GDE was not significant. Consequently, this GDE continues to allow a sufficient rate of CO_2 transfer to the catalyst sites to maintain good CO_2 selectivity (illustrated in Fig. 5f).

Another effect we observed related to differences in the structures of 29AA and 36BB and the high rates of liquid flooding was that more AgNPs were lost from the 29AA than from the 36BB catalyst after the electrochemical tests. The transport of AgNPs from the 29AA is evident in the EDS map of Ag in Fig. 5e (bottom) compared to Fig. 4. The loss of catalyst from 29AA could be another contributor to the low CO_2RR selectivity. Additionally, Fig. 5e shows that the CL of 36BB sustained its layered structure due to the MPL. Our result of the role of MPL on the performance of CO_2RR, is consistent with Kim et al. who also reported the critical role of the MPL in developing a well-defined CL structure [25].

The capacity of the MPL to mitigate flooding originates from this layer's hydrophobicity (Fig. 3g) and small-sized pores (Fig. 3f) [44,45]. However, the wetting properties of the electrode layer change during exposure to CO_2RR conditions due to the degradation of PTFE under negative potential [10,46]. For example, Niu et al. report a fall in hydrophobicity of a Cu-particle coated GDE after CO_2RR [47]. To understand how the wettability of the MPL changed during our CO_2RR experiments, we measured the contact angles on 29AA and 36BB GDEs after 30 min and 60 min of CO_2RR at a current density of 150 mA cm^{-2}. Fig. 6Error! Reference source not found.a show the hydrophobicity of both GDEs drops after exposure to CO_2RR conditions, and this change is more significant on 29AA GDE. For 29AA GDE, the apparent water contact angle decreased from 133.9 ± 2.5° before treatment to 82.2 ± 0.1° after 30 min treatment and 69.0 ± 4.3° after 60 min. This loss of hydrophobicity will lead to greater liquid flooding into the GDE. We also tested the apparent contact angles using the 0.5 M $KHCO_3$ aqueous droplets, and the results (Fig. S6a) show a similar trend to the results presented in Fig. 6a.

As a control measurement, we performed the same time-based experiment with GDLs 29AA and 36BB without AgNPs. Fig. 6b shows the contact angles on GDLs without catalysts also fell with longer exposure times in the electrolyser. Again, this treatment had a more profound impact on the wettability of 29AA than on 36BB. Additionally, we found that increasing the current density leads to a more significant loss of the hydrophobicity of the electrode surface (Fig. S6b). A similar downtrend of hydrophobicity was observed by Shi et al. [48] Two of the

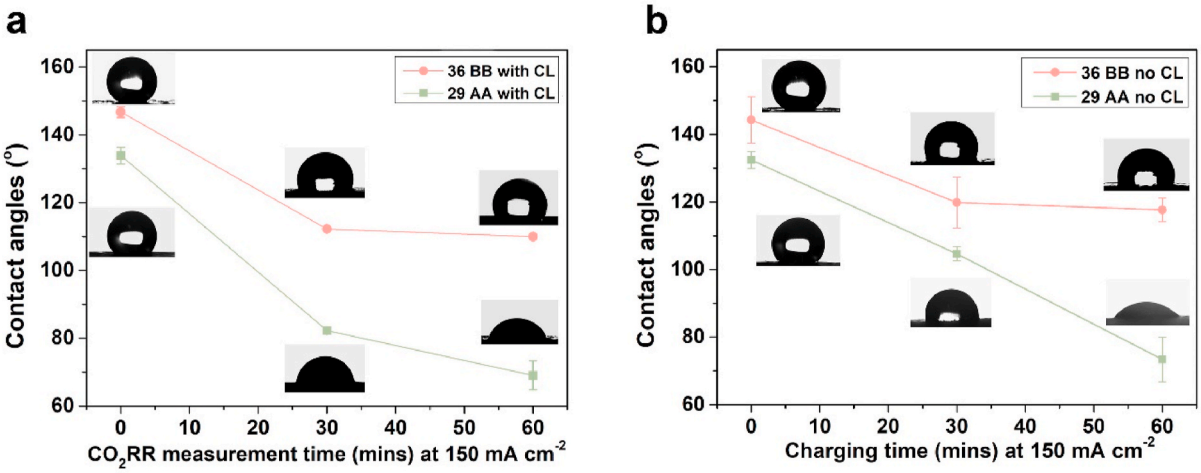

Fig. 6. (a) Sessile drop water apparent contact angles change of the GDEs and (b) only GDLs depend on measure time. All tested on the MPL side. The error bars represent the standard deviation of at least three independent measurements.

main factors for the loss of hydrophobicity are (i) electrowetting phenomena allow the electrolyte to spread more evenly when there is a stronger electrical field [49], and (ii) at the higher current density conditions the PTFE in the MPL is more likely to degrade [10].

3.4. The effect of microporous layer thickness on CO_2RR

The next part of our study examined how the thickness of the MPL affects the CO_2RR performance of AgNP-decorated GDEs using Sigracet gas diffusion layers 22BB and 39BB for direct comparisons in this section. Fig. 3e shows the MPL thickness of 22BB is similar to 36BB reported in the previous section, and the MPL of 39BB is the thickest layer of these

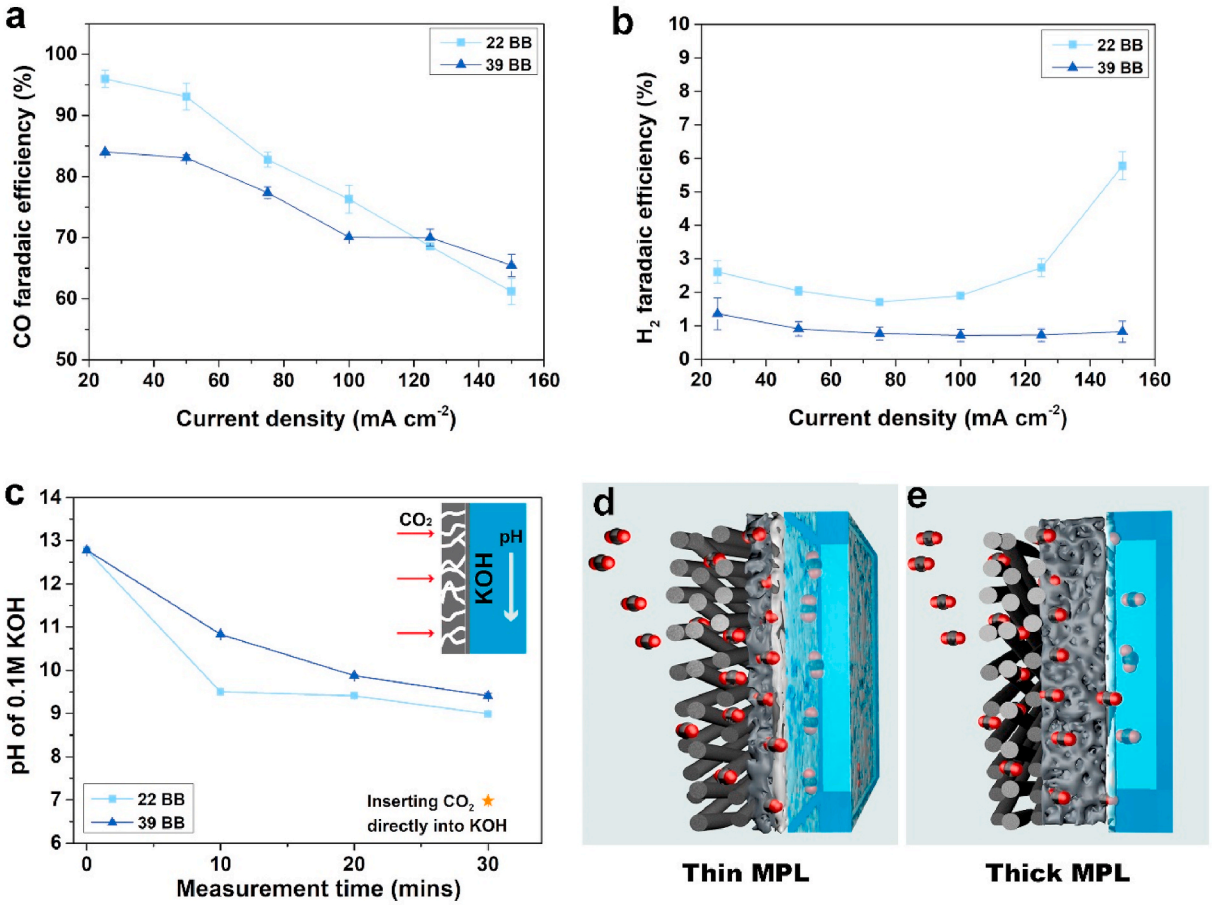

Fig. 7. Selectivity of 22BB(thin MPL) and 39BB(thick MPL) GDEs on CO_2RR: (a) FE_{CO} and (b) FE_{H2} depend on current density; (c) The pH of 0.1 M KOH from the effluent catholyte depends on time after 60 sccm CO_2 diffuse through the GDEs within the flow cell without charge; Illustration of the gas transport mechanism in (d) 22 BB and (e) 39BB. The error bars represent the standard deviation of at least three independent measurements.

commercial GDLs (32% thicker than the MPL of 22BB) with same CFS. Fig. 7a shows the FE_{CO} of 22BB with AgNPs is higher than the 39BB AgNP electrode at current densities lower than 125 mA cm^{-2}. For example, at 25 mA cm^{-2}, the FE_{CO} = 96% over the 22BB GDE, FE_{CO} = 95% over 36BB GDE, and FE_{CO} = 83% over the 39BB GDE. The CO selectivity falls at higher current densities for these GDEs, but the differences between FE_{CO} of the two GDEs fall at high current densities. When the current densities are greater than 125 mA cm^{-2}, the 39BB GDE with the thick MPL has a higher CO selectivity than the 29AA GDE. The trend in CO selectivity we observed here is similar to that in Fig. 5a for comparing 39BB GDE to 36BB GDE's CO selectivity. Notably, the GDE 39BB appears to be more effective at suppressing the HER than the 22BB GDE at high current densities (Fig. 7b).

We postulate that the high CO selectivity over GDE with a thin MPL at low current densities is related to the availability of CO_2. As shown in Fig. 4f, the permeance of CO_2 through the 22BB GDE is almost two-fold of the permeance through GDE 39BB. This permeance result indicates that the GDL with a thinner MPL has a lower resistance to CO_2 transport, likely because of shorter diffusion path length through the MPL than the thick MPL of 39BB [50]. To test if these permeance results translated to a similar trend when there was electrolyte at one side of the GDE (i.e., approximate the conditions for CO_2 transport during CO_2RR), we conducted an experiment with gas and 0.1 M KOH catholyte flowing in the electrolyser but no applied current or voltage, and measured pH of the catholyte leaving the electrolyser. Here we used KOH instead of $KHCO_3$ because the pH of the KOH is more sensitive to carbonation with CO_2 dissolved than $KHCO_3$ that induces buffering effect [51]. The change in pH of the KOH stream can represent the rate of diffusion of CO_2 through the GDE. Fig. 7c shows the pH of the catholyte effluent from the 22BB GDE electrolyser was lower than from the 39BB GDE. The higher flux of CO_2 through the 22BB GDE should enhance the local CO_2 availability at the interface between CL and catholyte (illustrated in Fig. 7d and e). This observation may explain why FE_{CO} was higher for 22BB GDE than 39BB at low current densities.

At high current densities than 100 mA cm^{-2}, we observed that the catholyte seepage rate became more severe over 22BB GDE than 39BB GDEs, as shown in Fig. 8a. The electrode flooding situation is more severe as the thickness of the MPL decreases. Mohsen et al. [52] reported a similar trend in PEM fuel cells in experiments using a high-speed camera to observe the liquid seepage. Similarly, we measured that the ECSA (Electrochemical Surface Area see Supporting Information for procedure. This ECSA is a measure of total electrochemical surface area of the GDE including the Ag catalyst, carbon black, MPL and support) of 22BB of 3.30 cm^2 mg^{-1} is larger than the 2.76 cm^2 mg^{-1} of 39BB as shown in Fig. S9. For completeness, we included a similar analysis of ECSA and capacitive current for 29AA and 36BB in the Support Information Fig. S7. The 22BB and 39BB ECSA results suggests more surface area was wetted in the 22BB GDE with thinner MPL than the 39BB with the thicker GDE.

To further probe the relations between the flooding and CO_2 permeance, we compared the CO_2 permeance of these two GDLs before and after CO_2RR conditioning at 150 mA cm^{-2} for 30 min. The drop in CO_2 permeance after GDE use in the electrolyser, shown in Fig. 8d, is likely due to the precipitation of potassium carbonates or bicarbonates salts from the catholyte in flooded electrode pores. This hypothesis is supported by the elements in the EDS mapping in Fig. 4e. The salt

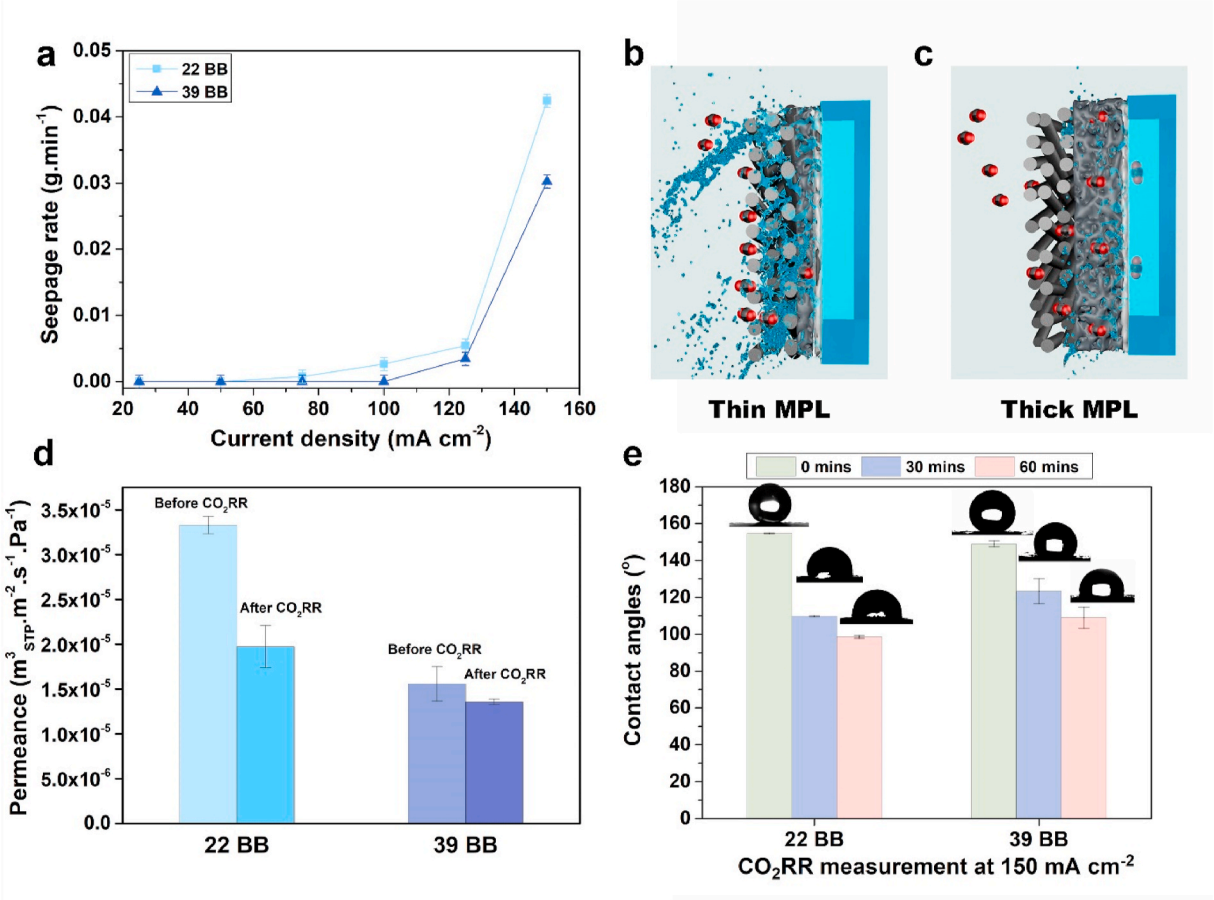

Fig. 8. (a) Seepage rate change of GDEs; (b, c) Illustrations of how MPL thickness influence the prevention of flooding; (d) Permeance comparison between origin GDEs and GDEs after 30 min CO2RR measurement at 150 mA cm^{-2}. (e) Sessile drop water contact angles change of the GDEs depends on electrolyzing time, all tested on the MPL side; The error bars represent the standard deviation of at least three independent measurements.

precipitation inside GDE due to high local pH was observed by Leonard et al. [53], who proposed that the carbonate salt precipitation leads to GDE failure and retards CO_2 transport. More importantly, the treated 39BB GDE exhibits comparable CO_2 permeance to the treated 22BB GDE, i.e., the thicker MPL is more resistant to the negative impact of the flooding and salt precipitation than the thinner MPL. The apparent contact angles measurement, as shown in Fig. 8e for water droplets and Fig. S8 0.5 M $KHCO_3$ droplets, also indicates the loss of apparent hydrophobicity in both MPLs, which could partially contribute to the flooding over the GDLs.

Our results demonstrate that the CO_2RR selectivity of GDEs depends on the MPL thickness due to effects of resistances to gas transfer and mitigation of liquid flooding. The resistance for the transport of the fluid (e.g., gas or electrolyte) increases with the thickness of the MPL. At low current densities (<125 mA cm^{-2}) where the electrolyte flooding is not severe, a thin MPL could allow a high local CO_2 availability at the catalyst surface and therefore a high CO_2RR selectivity. At high current densities (125 and 150 mA cm^{-2}) where electrolyte flooding becomes a critical issue, a thicker MPL could help resist the negative impacts of the electrolyte flooding and provides pathways for gas transport, which could sustain CO_2 availability at the CL and improve the CO_2RR selectivity.

4. Conclusions

In summary, we investigated the role of the microporous layer on gas and liquid in the GDE cathode, and its impact on the performance of CO_2RR in a gas-fed flow cell electrolyser. By monitoring the catholyte seepage rate during the CO_2 electrochemical reduction in a flow cell, we observed the relationship between the electrolyte flooding and CO_2RR selectivity. Our results demonstrate the important role of the MPL in preventing electrolyte flooding and supporting the catalyst layer. We found that because the transport resistance for both the gas and liquid increases with the thickness of MPL at low current density (<125 mA cm^{-2}) a thin MPL allows a high local CO_2 concentration at the interface between the CL and electrolyte. However, importantly, at current densities above 125 mA cm^{-2} a thicker MPL helps to suppress electrolyte flooding and allow the GDE to operate as designed to maintain CO_2RR selectivity to CO. Our work provides new insights to advance the carbon-based GDEs via modulating the structure of the MPL.

CRediT authorship contribution statement

Yuming Wu: Investigation, Conceptualization, Methodology, Software, Validation, Visualization, Formal analysis, Writing – original draft. **Sahil Garg:** Conceptualization, Methodology. **Mengran Li:** Conceptualization, Methodology, Supervision, Writing – review & editing. **Mohamed Nazmi Idros:** Investigation, Software. **Zhiheng Li:** Visualization. **Rijia Lin:** Investigation. **Jian Chen:** Software. **Guoxiong Wang:** Conceptualization, Funding acquisition, Supervision. **Thomas E. Rufford:** Conceptualization, Funding acquisition, Project administration, Supervision, Writing – review & editing.

Declaration of competing interest

The authors declare that they have no known competing financial interests or personal relationships that could have appeared to influence the work reported in this paper.

Acknowledgments

This research project received funding through a UQ Foundation Research Excellence Award and Australian Research Council (ARC) Linkage Project LP160101729 with the HBIS Group, China. Y. Wu, S. Garg, and M.N. Idros acknowledge the financial support provided by the UQ Research Training Program (RTP) scholarship. We acknowledge the facilities, and the scientific and technical assistance, of the Microscopy Australia Facility at the Centre for Microscopy and Microanalysis (CMM), The University of Queensland. The authors appreciate Dr. Jinxuan Zhang for his help in MIP measurement.

Appendix A. Supplementary data

Supplementary data to this article can be found online at https://doi.org/10.1016/j.jpowsour.2022.230998.

References

[1] H.B. Yang, S.-F. Hung, S. Liu, K. Yuan, S. Miao, L. Zhang, X. Huang, H.-Y. Wang, W. Cai, R. Chen, J. Gao, X. Yang, W. Chen, Y. Huang, H.M. Chen, C.M. Li, T. Zhang, B. Liu, Atomically dispersed Ni(i) as the active site for electrochemical CO2 reduction, Nat. Energy 3 (2) (2018) 140–147, https://doi.org/10.1038/s41560-017-0078-8.

[2] Y. Hori, H. Wakebe, T. Tsukamoto, O. Koga, Electrocatalytic process of CO selectivity in electrochemical reduction of CO2 at metal electrodes in aqueous media, Electrochim. Acta 39 (11) (1994) 1833–1839, https://doi.org/10.1016/0013-4686(94)85172-7.

[3] P. De Luna, C. Hahn, D. Higgins, S.A. Jaffer, T.F. Jaramillo, E.H. Sargent, What would it take for renewably powered electrosynthesis to displace petrochemical processes? Science 364 (6438) (2019) https://doi.org/10.1126/science.aav3506 eaav3506.

[4] D.M. Weekes, D.A. Salvatore, A. Reyes, A. Huang, C.P. Berlinguette, Electrolytic CO2 reduction in a flow cell, Acc. Chem. Res. 51 (4) (2018) 910–918, https://doi.org/10.1021/acs.accounts.8b00010.

[5] Z.D. Dong, L.J. Long, Q.S. Zhang, Recent advances in inorganic heterogeneous electrocatalysts for reduction of carbon dioxide, Adv. Mater. 28 (18) (2016) 3423–3452, https://doi.org/10.1002/adma.201504766.

[6] T.N. Nguyen, C.-T. Dinh, Gas diffusion electrode design for electrochemical carbon dioxide reduction, Chem. Soc. Rev. 49 (21) (2020) 7488–7504, https://doi.org/10.1039/D0CS00230E.

[7] R.I. Masel, Z. Liu, H. Yang, J.J. Kaczur, D. Carrillo, S. Ren, D. Salvatore, C. P. Berlinguette, An industrial perspective on catalysts for low-temperature CO2 electrolysis, Nat. Nanotechnol. 16 (2) (2021) 118–128, https://doi.org/10.1038/s41565-020-00823-x.

[8] G. Díaz-Sainz, M. Alvarez-Guerra, A. Irabien, Continuous electrochemical reduction of CO2 to formate: comparative study of the influence of the electrode configuration with Sn and Bi-based electrocatalysts, Molecules 25 (19) (2020), https://doi.org/10.3390/molecules25194457.

[9] G. Díaz-Sainz, M. Alvarez-Guerra, B. Ávila-Bolívar, J. Solla-Gullón, V. Montiel, A. Irabien, Improving trade-offs in the figures of merit of gas-phase single-pass continuous CO2 electrocatalytic reduction to formate, Chem. Eng. J. 405 (2021) 126965, https://doi.org/10.1016/j.cej.2020.126965.

[10] T. Burdyny, W.A. Smith, CO2 reduction on gas-diffusion electrodes and why catalytic performance must be assessed at commercially-relevant conditions, Energy Environ. Sci. 12 (5) (2019) 1442–1453, https://doi.org/10.1039/C8EE03134G.

[11] Q. Wang, H. Dong, H. Yu, H. Yu, Enhanced performance of gas diffusion electrode for electrochemical reduction of carbon dioxide to formate by adding polytetrafluoroethylene into catalyst layer, J. Power Sources 279 (2015) 1–5, https://doi.org/10.1016/j.jpowsour.2014.12.118.

[12] Z. Lu, M.M. Daino, C. Rath, S.G. Kandlikar, Water management studies in PEM fuel cells, part III: dynamic breakthrough and intermittent drainage characteristics from GDLs with and without MPLs, Int. J. Hydrogen Energy 35 (9) (2010) 4222–4233, https://doi.org/10.1016/j.ijhydene.2010.01.012.

[13] N.T. Nesbitt, T. Burdyny, H. Simonson, D. Salvatore, D. Bohra, R. Kas, W.A. Smith, Liquid–Solid boundaries dominate activity of CO2 reduction on gas-diffusion electrodes, ACS Catal. 10 (23) (2020) 14093–14106, https://doi.org/10.1021/acscatal.0c03319.

[14] R. Shi, Z. Wang, Y. Zhao, G.I.N. Waterhouse, Z. Li, B. Zhang, Z. Sun, C. Xia, H. Wang, T. Zhang, Room-temperature electrochemical acetylene reduction to ethylene with high conversion and selectivity, Nat. Catal. 4 (7) (2021) 565–574, https://doi.org/10.1038/s41929-021-00640-y.

[15] A.Z. Weber, R.L. Borup, R.M. Darling, P.K. Das, T.J. Dursch, W. Gu, D. Harvey, A. Kusoglu, S. Litster, M.M. Mench, R. Mukundan, J.P. Owejan, J.G. Pharoah, M. Secanell, I.V. Zenyuk, A critical review of modeling transport phenomena in polymer-electrolyte fuel cells, J. Electrochem. Soc. 161 (12) (2014) F1254–F1299, https://doi.org/10.1149/2.0751412jes.

[16] M.E. Leonard, M.J. Orella, N. Aiello, Y. Román-Leshkov, A. Forner-Cuenca, F. R. Brushett, Editors' choice—flooded by success: on the role of electrode wettability in CO2 electrolyzers that generate liquid products, J. Electrochem. Soc. 167 (12) (2020) 124521, https://doi.org/10.1149/1945-7111/abaa1a.

[17] J. Qiao, Y. Liu, F. Hong, J. Zhang, A review of catalysts for the electroreduction of carbon dioxide to produce low-carbon fuels, Chem. Soc. Rev. 43 (2) (2014) 631–675.

[18] M. Li, S. Garg, X. Chang, L. Ge, L. Li, M. Konarova, T.E. Rufford, V. Rudolph, G. Wang, Toward excellence of transition metal-based catalysts for CO2 electrochemical reduction: an overview of strategies and rationales, Small Methods 4 (7) (2020) 2000033, https://doi.org/10.1002/smtd.202000033.

[19] M. Li, M.N. Idros, Y. Wu, S. Garg, S. Gao, R. Lin, H. Rabiee, Z. Li, L. Ge, T. E. Rufford, Z. Zhu, L. Li, G. Wang, Unveiling the effects of dimensionality of tin oxide-derived catalysts on CO2 reduction by using gas-diffusion electrodes, React. Chem. Eng. (2021), https://doi.org/10.1039/D0RE00396D.
[20] M. Li, X. Tian, S. Garg, T.E. Rufford, P. Zhao, Y. Wu, A.J. Yago, L. Ge, V. Rudolph, G. Wang, Modulated Sn oxidation states over a Cu2O-derived substrate for selective electrochemical CO2 reduction, ACS Appl. Mater. Interfaces 12 (20) (2020) 22760–22770, https://doi.org/10.1021/acsami.0c00412.
[21] S. Park, J.-W. Lee, B.N. Popov, A review of gas diffusion layer in PEM fuel cells: materials and designs, Int. J. Hydrogen Energy 37 (7) (2012) 5850–5865, https://doi.org/10.1016/j.ijhydene.2011.12.148.
[22] M. Mortazavi, K. Tajiri, Liquid water breakthrough pressure through gas diffusion layer of proton exchange membrane fuel cell, Int. J. Hydrogen Energy 39 (17) (2014) 9409–9419, https://doi.org/10.1016/j.ijhydene.2014.03.238.
[23] J. Lee, J. Hinebaugh, A. Bazylak, Synchrotron X-ray radiographic investigations of liquid water transport behavior in a PEMFC with MPL-coated GDLs, J. Power Sources 227 (2013) 123–130, https://doi.org/10.1016/j.jpowsour.2012.11.006.
[24] A. Nishimura, K. Yamamoto, T. Okado, Y. Kojima, M. Hirota, M.L. Kolhe, Impact analysis of MPL and PEM thickness on temperature distribution within PEFC operating at relatively higher temperature, Energy 205 (2020) 117875, https://doi.org/10.1016/j.energy.2020.117875.
[25] B. Kim, F. Hillman, M. Ariyoshi, S. Fujikawa, P.J.A. Kenis, Effects of composition of the micro porous layer and the substrate on performance in the electrochemical reduction of CO2 to CO, J. Power Sources 312 (2016) 192–198, https://doi.org/10.1016/j.jpowsour.2016.02.043.
[26] W.-H. Cheng, M.H. Richter, I. Sullivan, D.M. Larson, C. Xiang, B.S. Brunschwig, H. A. Atwater, CO2 reduction to CO with 19% efficiency in a solar-driven gas diffusion electrode flow cell under outdoor solar illumination, ACS Energy Lett. 5 (2) (2020) 470–476, https://doi.org/10.1021/acsenergylett.9b02576.
[27] D. Kopljar, A. Inan, P. Vindayer, N. Wagner, E. Klemm, Electrochemical reduction of CO2 to formate at high current density using gas diffusion electrodes, J. Appl. Electrochem. 44 (10) (2014) 1107–1116, https://doi.org/10.1007/s10800-014-0731-x.
[28] S. Verma, X. Lu, S. Ma, R.I. Masel, P.J.A. Kenis, The effect of electrolyte composition on the electroreduction of CO2 to CO on Ag based gas diffusion electrodes, Phys. Chem. Chem. Phys. 18 (10) (2016) 7075–7084, https://doi.org/10.1039/C5CP05665A.
[29] S. Sen, S.M. Brown, M. Leonard, F.R. Brushett, Electroreduction of carbon dioxide to formate at high current densities using tin and tin oxide gas diffusion electrodes, J. Appl. Electrochem. 49 (9) (2019) 917–928, https://doi.org/10.1007/s10800-019-01332-z.
[30] G. Lin, T.V. Nguyen, Effect of thickness and hydrophobic polymer content of the gas diffusion layer on electrode flooding level in a PEMFC, J. Electrochem. Soc. 152 (10) (2005) A1942, https://doi.org/10.1149/1.2006487.
[31] M.N. Idros, Contact Angle Measurement GitHub, GitHub, 2020.
[32] L. Ge, Z. Zhu, F. Li, S. Liu, L. Wang, X. Tang, V. Rudolph, Investigation of gas permeability in carbon nanotube (CNT)−Polymer matrix membranes via modifying CNTs with functional groups/metals and controlling modification location, J. Phys. Chem. C 115 (14) (2011) 6661–6670, https://doi.org/10.1021/jp1120965.
[33] Y.C. Tan, K.B. Lee, H. Song, J. Oh, Modulating local CO2 concentration as a general strategy for enhancing C−C coupling in CO2 electroreduction, Joule 4 (5) (2020) 1104–1120, https://doi.org/10.1016/j.joule.2020.03.013.
[34] H. Ito, Y. Heo, M. Ishida, A. Nakano, S. Someya, T. Munakata, Application of a self-supporting microporous layer to gas diffusion layers of proton exchange membrane fuel cells, J. Power Sources 342 (2017) 393–404, https://doi.org/10.1016/j.jpowsour.2016.12.064.
[35] R. Flückiger, S.A. Freunberger, D. Kramer, A. Wokaun, G.G. Scherer, F.N. Büchi, Anisotropic, effective diffusivity of porous gas diffusion layer materials for PEFC, Electrochim. Acta 54 (2) (2008) 551–559, https://doi.org/10.1016/j.electacta.2008.07.034.
[36] J. Moorhouse, Modern Chlor-Alkali Technology, Wiley, 2008.
[37] F. Hendricks, J. Chamier, S. Tanaka, Membrane electrode assembly performance of a standalone microporous layer on a metallic gas diffusion layer, J. Power Sources 464 (2020) 228222, https://doi.org/10.1016/j.jpowsour.2020.228222.
[38] Y.R.J. Thomas, A. Benayad, M. Schroder, A. Morin, J. Pauchet, New method for super hydrophobic treatment of gas diffusion layers for proton exchange membrane fuel cells using electrochemical reduction of diazonium salts, ACS Appl. Mater. Interfaces 7 (27) (2015) 15068–15077, https://doi.org/10.1021/acsami.5b04428.
[39] H. Ungan, A. Bayrakçeken Yurtcan, PEMFC catalyst layer modification with the addition of different amounts of PDMS polymer in order to improve water management, Int. J. Energy Res. 43 (11) (2019) 5946–5958, https://doi.org/10.1002/er.4704.
[40] F.P. García de Arquer, C.-T. Dinh, A. Ozden, J. Wicks, C. McCallum, A.R. Kirmani, D.-H. Nam, C. Gabardo, A. Seifitokaldani, X. Wang, Y.C. Li, F. Li, J. Edwards, L. J. Richter, S.J. Thorpe, D. Sinton, E.H. Sargent, CO2 electrolysis to multicarbon products at activities greater than 1 A cm− 2, Science 367 (6478) (2020) 661, https://doi.org/10.1126/science.aay4217.
[41] L. Fan, C. Xia, P. Zhu, Y. Lu, H. Wang, Electrochemical CO2 reduction to high-concentration pure formic acid solutions in an all-solid-state reactor, Nat. Commun. 11 (1) (2020) 3633, https://doi.org/10.1038/s41467-020-17403-1.
[42] T.-T. Zhuang, Y. Pang, Z.-Q. Liang, Z. Wang, Y. Li, C.-S. Tan, J. Li, C.T. Dinh, P. De Luna, P.-L. Hsieh, T. Burdyny, H.-H. Li, M. Liu, Y. Wang, F. Li, A. Proppe, A. Johnston, D.-H. Nam, Z.-Y. Wu, Y.-R. Zheng, A.H. Ip, H. Tan, L.-J. Chen, S.-H. Yu, S.O. Kelley, D. Sinton, E.H. Sargent, Copper nanocavities confine intermediates for efficient electrosynthesis of C3 alcohol fuels from carbon monoxide, Nat. Catal. 1 (12) (2018) 946–951, https://doi.org/10.1038/s41929-018-0168-4.
[43] H. Yi, F. Jia, Y. Zhao, W. Wang, S. Song, H. Li, C. Liu, Surface wettability of montmorillonite (0 0 1) surface as affected by surface charge and exchangeable cations: a molecular dynamic study, Appl. Surf. Sci. 459 (2018) 148–154, https://doi.org/10.1016/j.apsusc.2018.07.216.
[44] M. Han, S.H. Chan, S.P. Jiang, Development of carbon-filled gas diffusion layer for polymer electrolyte fuel cells, J. Power Sources 159 (2) (2006) 1005–1014, https://doi.org/10.1016/j.jpowsour.2005.12.003.
[45] A.Z. Weber, J. Newman, Effects of microporous layers in polymer electrolyte fuel cells, J. Electrochem. Soc. 152 (4) (2005) A677, https://doi.org/10.1149/1.1861194.
[46] H. Yang, Y.-w. Hu, J.-j. Chen, M.S. Balogun, P.-p. Fang, S. Zhang, J. Chen, Y. Tong, Intermediates adsorption engineering of CO2 electroreduction reaction in highly selective heterostructure Cu-based electrocatalysts for CO production, Adv. Energy Mater. 9 (27) (2019) 1901396, https://doi.org/10.1002/aenm.201901396.
[47] Z.-Z. Niu, F.-Y. Gao, X.-L. Zhang, P.-P. Yang, R. Liu, L.-P. Chi, Z.-Z. Wu, S. Qin, X. Yu, M.-R. Gao, Hierarchical copper with inherent hydrophobicity mitigates electrode flooding for high-rate CO2 electroreduction to multicarbon products, J. Am. Chem. Soc. (2021), https://doi.org/10.1021/jacs.1c01190.
[48] R. Shi, J. Guo, X. Zhang, G.I.N. Waterhouse, Z. Han, Y. Zhao, L. Shang, C. Zhou, L. Jiang, T. Zhang, Efficient wettability-controlled electroreduction of CO2 to CO at Au/C interfaces, Nat. Commun. 11 (1) (2020) 3028, https://doi.org/10.1038/s41467-020-16847-9.
[49] M. Li, M.N. Idros, Y. Wu, T. Burdyny, S. Garg, X.S. Zhao, G. Wang, T.E. Rufford, The role of electrode wettability in electrochemical reduction of carbon dioxide, J. Mater. Chem. (2021), https://doi.org/10.1039/D1TA03636J.
[50] R.W. Baker, J.G. Wijmans, Y. Huang, Permeability, permeance and selectivity: a preferred way of reporting pervaporation performance data, J. Membr. Sci. 348 (1) (2010) 346–352, https://doi.org/10.1016/j.memsci.2009.11.022.
[51] K.C. Bedin, A.C. Martins, A.L. Cazetta, O. Pezoti, V.C. Almeida, KOH-activated carbon prepared from sucrose spherical carbon: adsorption equilibrium, kinetic and thermodynamic studies for Methylene Blue removal, Chem. Eng. J. 286 (2016) 476–484, https://doi.org/10.1016/j.cej.2015.10.099.
[52] M. Afra, M. Nazari, M.H. Kayhani, M. Sharifpur, J.P. Meyer, 3D experimental visualization of water flooding in proton exchange membrane fuel cells, Energy 175 (2019) 967–977, https://doi.org/10.1016/j.energy.2019.03.128.
[53] M.E. Leonard, L.E. Clarke, A. Forner-Cuenca, S.M. Brown, F.R. Brushett, Investigating electrode flooding in a flowing electrolyte, gas-fed carbon dioxide electrolyzer, ChemSusChem 13 (2) (2020) 400–411, https://doi.org/10.1002/cssc.201902547.